Materialia 8 (2019) 100485

Contents lists available at ScienceDirect

Materialia

journal homepage: www.elsevier.com/locate/mtla

Full Length Article

Extraordinary ductility and strain hardening of $Cr_{26}Mn_{20}Fe_{20}Co_{20}Ni_{14}$ TWIP high-entropy alloy by cooperative planar slipping and twinning

Xuzhou Gao[a,1], Yiping Lu[b,c,1,*], Jizi Liu[d,*], Jun Wang[c], Tongming Wang[b], Yonghao Zhao[a,*]

[a] Nano and Heterogeneous Materials Center, School of Materials Science and Engineering, Nanjing University of Science and Technology, Nanjing 210094, China
[b] Key Laboratory of Solidification Control and Digital Preparation Technology (Liaoning Province), School of Materials Science and Engineering, Dalian University of Technology, Dalian 116024, China
[c] State Key Laboratory of Solidification Processing, Northwestern Polytechnical University, Xi'an 710072, China
[d] Herbert Gleiter Institute of Nanoscience, Nanjing University of Science and Technology, Nanjing 210094, China

ARTICLE INFO

Keywords:
High entropy alloys
Strength and ductility
Strain hardening
Stacking fault energy
Twinning and planar slipping

ABSTRACT

High-entropy alloys (HEAs), containing at least five major metal elements in equal or near equal atomic ratios, have drawn increasing attention because they open entirely new materials avenues for designing alloys with exceptional properties. In the literature, a well-studied equiatomic, face-centered cubic CrMnFeCoNi HEA reportedly exhibits a yield strength of 410 MPa and a ductility of 57% as well as a deformation mechanism of dislocation slip at room temperature [B. Gludovatz, et al., Science, 345 (2014) 1153–1158]. Some recent works also observed that twinning actually happens more or less in the equiatomic CrMnFeCoNi alloy at room temperature [Z.J. Zhang, et al., Nature Comm. 6 (2015) 10143]. In this study, we prepared a non-equiatomic, face-centered cubic $Cr_{26}Mn_{20}Fe_{20}Co_{20}Ni_{14}$ HEA with a comparatively low stacking fault energy (SFE) by making an appropriate adjustment of the composition ratio. Our HEA has a yield strength of 180 MPa and a high strain hardening exponent, *n*, of 0.46 as well as a higher ductility (73%) than those of the CrMnFeCoNi alloy. Investigation of the deformation mechanisms at specific strain levels revealed a clear transition from planar slip dislocations in the initial deformation stage to twinning at high tensile strain. Cooperative planar slipping and twinning resulted from the comparatively low SFE and were responsible to the extraordinary ductility and strain hardening capability. Besides deformation twins, other hardening mechanisms including forest dislocations, sessile Lomer–Cottrell locks, dislocation-stacking fault interactions, sub-grain boundary and phase boundary were revealed.

1. Introduction

In the past decade, a new concept of high-entropy alloys (HEAs), or multi-component alloys, has attracted increasing attention due to its inherent compositional variability for designing novel materials with exceptional properties [1–4]. HEAs, consisting of at least five elements in equal or near equal atomic ratios [5–7], maximize the entropy of mixing with the aim of producing single-phase face-centered cubic (FCC), body-centered cubic (BCC), and hexagonal close-packed (HCP) solid solutions [8–10]. Among various HEAs, the FCC HEAs possess excellent mechanical properties, especially at cryogenic temperatures, and are promising for industrial applications. A typical example is the equiatomic CrMnFeCoNi HEA, whose aspects such as vacancy motion [11], optimization of mechanical properties by thermomechanical treatments [12,13], texture evolution [12], and deformation mechanisms [13–15] have been extensively investigated. The alloy exhibits synergetic increases of ultimate tensile strength (from 750 to 1280 MPa) and ductility (from 56% to 70%) with decreasing temperature from 293 to 77 K. In addition, the fracture toughness remains approximately 200 MPa $m^{1/2}$ for crack initiation and 300 MPa $m^{1/2}$ for stable crack growth at 77 K [2]. Similar temperature-dependent mechanical properties were also reported in the medium-entropy alloy (MEA) CoCrNi [16]. One reason for the temperature dependencies of these properties is thought to be the transition of deformation mechanisms from planar slip dislocation at room temperature to mechanical nanoscale twinning at cryogenic temperatures [3,14]. Stacking fault (SF) energy is reported to decrease by 20%–60% when the temperature drops from 293 to 77 K [17]. The lower SF energy (SFE) at cryogenic temperature reduces the critical resolved shear stress (CRSS) for twinning, and therefore it promotes the twinning-induced plasticity (TWIP) effect. Generally, deformation mechanisms and SFE have the following relationships: (i) dislocation slip with SFEs larger than 60 mJ m^{-2}; (ii) twinning with SFEs between 20 and 60 mJ m^{-2};

* Corresponding authors.
E-mail addresses: luyiping@dlust.edu.cn (Y. Lu), jzliu@njust.edu.cn (J. Liu), yhzhao@njust.edu.cn (Y. Zhao).
[1] These authors contributed equally to this work.

https://doi.org/10.1016/j.mtla.2019.100485
Received 21 June 2019; Accepted 23 September 2019
Available online 25 September 2019

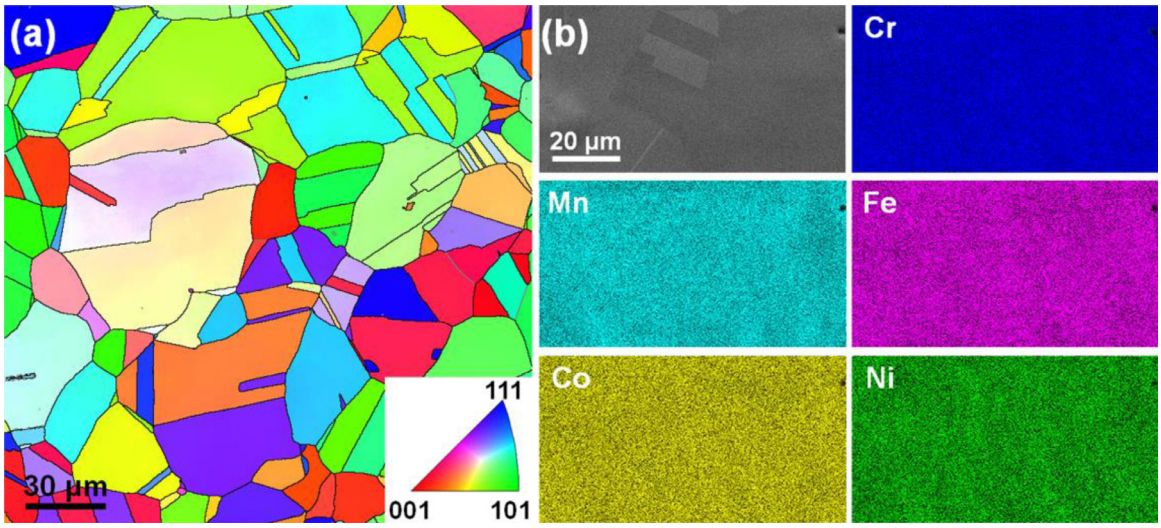

Fig. 1. Initial microstructures and compositional distributions of the $Cr_{26}Mn_{20}Fe_{20}Co_{20}Ni_{14}$ HEA. (a) An EBSD crystal orientation map showing the fully recrystallized microstructure. (b) SEM-EDS maps showing homogeneous distributions of Cr, Mn, Fe, Co, and Ni elements in the HEA.

and (iii) transformation from FCC to HCP phase, i.e., transformation-induced plasticity (TRIP), with SFEs lower than 20 mJ m^{-2} [18–21].

Compared with the extrinsic factor of temperature, the alloying composition is the intrinsic factor that affects the SFE, so introducing TWIP and even TRIP effects by lowering SFE via an appropriate adjustment of composition ratio is an effective strategy to optimize the mechanical properties of HEAs at room temperature. Raabe et al. have conducted related research on the quaternary FeMnCoCr system [2,22–24]. The $Fe_{40}Mn_{40}Co_{10}Cr_{10}$ HEA possesses comparable mechanical properties (yield strength of 240 MPa, ultimate tensile strength of 489 MPa, and total elongation of 58%) at room temperature to those of advanced FeMnC and FeMnAlC TWIP steels [21]. Furthermore, an optimum $Fe_{50}Mn_{30}Co_{10}Cr_{10}$ HEA has mechanical properties (yield strength of 330 MPa, ultimate tensile strength of 880 MPa, and total elongation of 73%) that are comparable to the CrMnFeCoNi alloy, resulting from a severe TRIP effect and a highly beneficial dynamic strain–stress partitioning effect on the two phases [2]. In addition, First-principles electronic structure calculations in conjunction with x-ray diffraction measurements revealed that the SFEs of HEAs decrease with the number of components, and can be further reduced by tailoring the atomic ratios of individual components [25]. For instance, the SFE of CrMnFeNiCo HEA is calculated as approximately 25 mJ m^{-2}, that of $Cr_{26}Mn_{20}Fe_{20}Co_{20}Ni_{14}$ HEA is as low as 3.5 mJ m^{-2} [25].

In this study, we prepared a non-equiatomic FCC $Cr_{26}Mn_{20}Fe_{20}Co_{20}Ni_{14}$ HEA by an appropriate adjustment of composition ratio to decrease SFE and promote twinning. Mechanical properties at room temperature were then tested and deformation mechanisms at different strain levels were revealed by systematic microstructural characterizations by transmission electron microscopy (TEM) and high-resolution transmission electron microscopy (HRTEM). Deformation twins, forest dislocations, and the interaction of glide dislocations with SFs as well as sessile Lomer–Cottrell locks were revealed as the main hardening mechanisms.

2. Experiments

Elemental Cr, Mn, Fe, Co, and Ni were used as raw materials, each having purity greater than 99.5%. The raw materials with the nominal composition of $Cr_{26}Mn_{20}Fe_{20}Co_{20}Ni_{14}$ were alloyed in a boron nitride (BN) crucible in a medium frequency vacuum induction melting furnace. Before it was placed in the furnace, the BN crucible was heated at 873 K for 1 h to remove water vapor. The furnace chamber was evacuated to 10^{-2} Pa and backfilled with argon to 0.06 MPa before the melting started. The liquid metal was held at 1823 K for 15 min and poured into a ZrO_2-coated MgO crucible (preheated at 873 K before casting). An IRTM-2CK infrared pyrometer was employed to monitor the temperature with an absolute accuracy of 2 K. The alloys were re-melted twice to ensure homogeneity. The as-cast $Cr_{26}Mn_{20}Fe_{20}Co_{20}Ni_{14}$ sample was hot-forged at 1000 °C to eliminate casting flaws, such as shrinkage cavities and equilibrium compositional segregation, and then annealed at 1000 °C for 8 h to achieve a recrystallized coarse-grained (CG) structure. A Walter + bai LFM 20 kN tensile testing machine was used for tensile testing at room temperature with a normal strain rate of 1×10^{-3} s^{-1}. The flat dog bone-shaped tensile samples had a gauge dimension of $20 \times 3 \times 2$ mm^3. The strain was measured using a standard non-contacting video extensometer. Three tensile specimens were measured to obtain reliable results.

Microstructure and composition analyses were carried out by means of electron back-scattered diffraction (EBSD), TEM, HRTEM, and energy-dispersive spectrometer (EDS) techniques. Specifically, EBSD mapping of specimens was conducted using a high-resolution field emission Carl Zeiss-Auriga-45-66 scanning electron microscope (SEM) equipped with a fully automatic Oxford Instruments Aztec 2.0 EBSD system (Channel 5 software). The EBSD specimens were mechanically polished and then electropolished in an electrolyte containing 90 vol% acetic acid and 10 vol% perchloric acid using a voltage of 35 V and polishing time of 1 min in a Buehler ElectroMet 4 polisher. The EBSD specimen was then used in EDS analysis. TEM observations were conducted in an FEI-Tecnai G^2 20 S-TWIN microscope operated at 200 kV. HRTEM was conducted in a Titan G^2 60–300 operated at 300 kV. The TEM specimens were prepared by grinding the deformed gauge part down to 50 μm thickness. TEM specimens with a thickness of approximately 50 μm were then punched into discs with a diameter of 3 mm and were electro-polished to an electron-transparent thickness in an aqueous electrolyte containing 10% perchloric acid, 20% glycerol, and 70% methanol at –20 °C via a twin jet electro-polishing system.

3. Results

3.1. Initial microstructures and compositional distributions

Fig. 1a shows EBSD mapping of the annealed $Cr_{26}Mn_{20}Fe_{20}Co_{20}Ni_{14}$ sample, which was composed of fully recrystallized equiaxed grains with the mean grain size of 50 μm and numerous annealing twins. By comparing the orientation map with the inverse pole figure (IPF) shown as an inset in Fig. 1a, one can conclude that the crystal orientations were random without any texture. A region containing a normal grain boundary (GB) and a twin boundary (TB) of the as-annealed alloy was prepared for

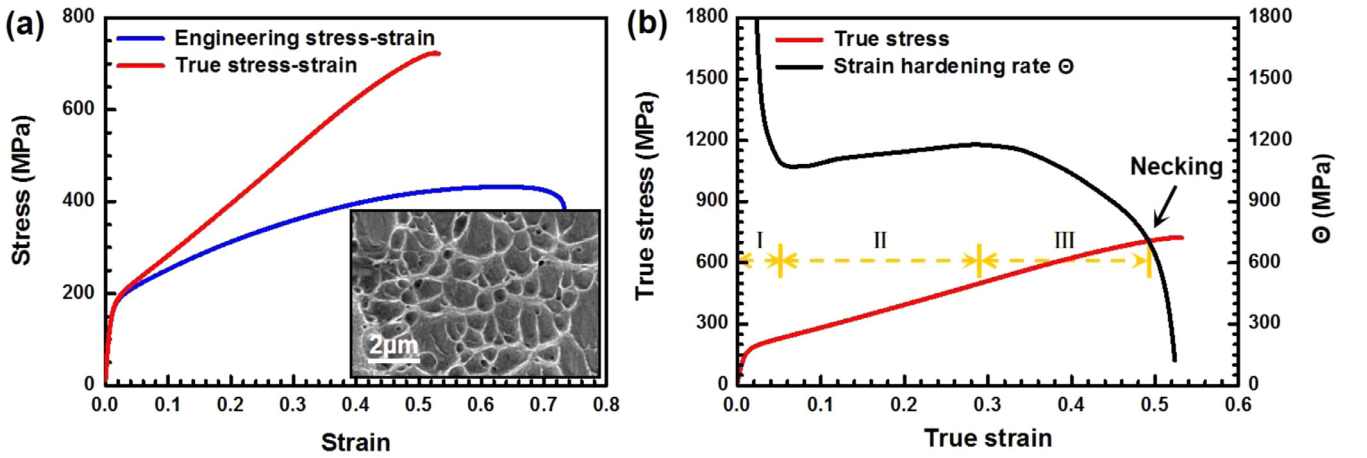

Fig. 2. Mechanical properties of $Cr_{26}Mn_{20}Fe_{20}Co_{20}Ni_{14}$ HEA at room temperature. (a) Tensile engineering and true stress–strain curves. Inset is the SEM image of the fracture surface with micrometer-sized dimples. (b) Strain hardening rate Θ versus true strain. Three stages could be distinguished, as marked along the yellow dashed line. (For interpretation of the references to colour in this figure legend, the reader is referred to the web version of this article.)

compositional homogeneity analysis by SEM-EDS, as shown in Fig. 1b. All the alloying elements (Cr, Mn, Fe, Co, Ni) were homogenously distributed without apparent elemental segregation or second phases, indicating that the HEA was a uniform and random solid solution. This is different from FeMn- and FeMnNi-based alloys in which Mn segregation at GBs are seen [26–28].

3.2. Tensile properties

Fig. 2 shows the tensile stress–strain and strain hardening rate curves of the $Cr_{26}Mn_{20}Fe_{20}Co_{20}Ni_{14}$ HEA at room temperature. The alloy had a yield strength of 180 ± 10 MPa, an ultimate tensile strength of 430 ± 15 MPa, and ductility of 73 ± 5%, which are comparable to those of CrMnFeCoNi [3,8], CrMnFeCo [2,22–24], and CrFeCoNi alloys [29]. The SEM image of the fracture surface as the inset in Fig. 2a reveals numerous dimples of ~1 μm, suggesting a tough fracture in the $Cr_{26}Mn_{20}Fe_{20}Co_{20}Ni_{14}$ HEA. Fig. 2b shows the corresponding strain hardening rate ($\sigma = K\varepsilon_p^n$, where σ is true stress, ε is true strain) with three distinct stages. In stage I ($\varepsilon < 6\%$), Θ was observed to decrease continuously due to the conventional transition from elastic to slip-dominated plastic deformation. In stage II ($6\% < \varepsilon < 29\%$), Θ increased to form a broad peak. In stage III ($\varepsilon = 29\%$), Θ decreased again until necking. The broad Θ peak of the $Cr_{26}Mn_{20}Fe_{20}Co_{20}Ni_{14}$ HEA was different from those of traditional materials with high SFE, such as Cu and Ni [30,31] that lack stage II, and was more remarkable than those of CrMnFeCoNi [3], $Fe_{40}Mn_{40}Co_{10}Cr_{10}$ [22], and $Fe_{50}Mn_{30}Co_{10}Cr_{10}$ [2], indicating a better strain hardening ability. In the literature, the Θ peak is usually caused by additional plastic deformation; for example, twinning or phase transformation in TRIP and TWIP steels [32], or further dislocation accumulation by complex stresses in gradient materials [33,34].

Another parameter used for evaluating strain hardening capability is the strain hardening exponent n, whose value could be simulated by the Hollomon and Ludwick equations, respectively, as shown below [35]:

$$\sigma = K\varepsilon_p^n \tag{1}$$

$$\sigma = \sigma_0 + K\varepsilon_p^n \tag{2}$$

where σ_0 is the yield stress, ε_p is true plastic strain, K is a strength coefficient representing the true stress when $\varepsilon_p = 1$. Fig. 3 shows experimental true stress–strain curves of $Cr_{26}Mn_{20}Fe_{20}Co_{20}Ni_{14}$ HEA and simulated curves by Hollomon and Ludwick equations at different deformation stages and Table 1 lists the simulated n values for different stages. The

Table 1
Simulated values of the strain hardening exponent n, the strengthening coefficient K, and yield strength σ_0 from Hollomon and Ludwick equations.

Specimens	Equation	Hollomon		Ludwick		
	Stages	K (MPa)	n	σ_0 (MPa)	K (MPa)	n
HEA	0–53%	895	0.46	143	1032	0.85
	I: 1%–6%	464	0.23	143	845	0.75
	II: 6%–29%	881	0.49	143	995	0.85
	III: 26%–49%	1141	0.66	143	1060	0.87

overall n of the $Cr_{26}Mn_{20}Fe_{20}Co_{20}Ni_{14}$ HEA was 0.46 by the Hollomon equation and 0.85 by the Ludwick equation. The high n value indicates a high strain hardening ability of the $Cr_{26}Mn_{20}Fe_{20}Co_{20}Ni_{14}$ HEA, comparable to TRIP and TWIP steels [36–38]. In stage I, n was 0.23 by the Hollomon equation and 0.75 by the Ludwick equation. In stage II, n reached 0.49 (Hollomon) and 0.85 (Ludwick). In stage III, n increased to 0.66 (Hollomon) and 0.87 (Ludwick), which are superior values among HEAs as well as TWIP and TRIP alloys [36–38]. Based on Hart's theory [39] and the Considère criterion [40], Θ contributed to high ductility because it can help delay necking and prolong elongation.

3.3. Deformation mechanisms

The strain hardening of metals results mainly from dislocation multiplication and interactions between dislocations and other lattice defects as well as themselves. To further reveal the underlying deformation mechanisms of the $Cr_{26}Mn_{20}Fe_{20}Co_{20}Ni_{14}$ HEA at different stages, TEM observations were performed. Fig. 4 shows TEM micrographs of $Cr_{26}Mn_{20}Fe_{20}Co_{20}Ni_{14}$ HEA, which were tensile deformed to different true strains (as marked in the lower right corner of each panel). Note that all the micrographs in Fig. 4 have the same magnification and the same contrast conditions, i.e., $\boldsymbol{g} = \langle 111 \rangle$, as indicated by white arrows in the upper right corners of the micrographs. When the specimen was tensile strained up to 2%, planar slips on two sets of {111} slip planes were activated from GBs, forming discontinuous slip traces due to the low density of dislocations. Moreover, a dislocation array with a high density of parallel dislocations was piled up at the boundary of annealing TB, as shown in the magnified inset in Fig. 4a. By increasing the true strain to 6%, a large number of parallel dislocation arrays were emitted from GBs, but still kept the features of planar slip. The stable piling up of dislocations under the unloading condition indicates the presence of a significant friction stress and a resistance of GBs to dislocation transmission or absorption [13]. In addition to the slip of parallel

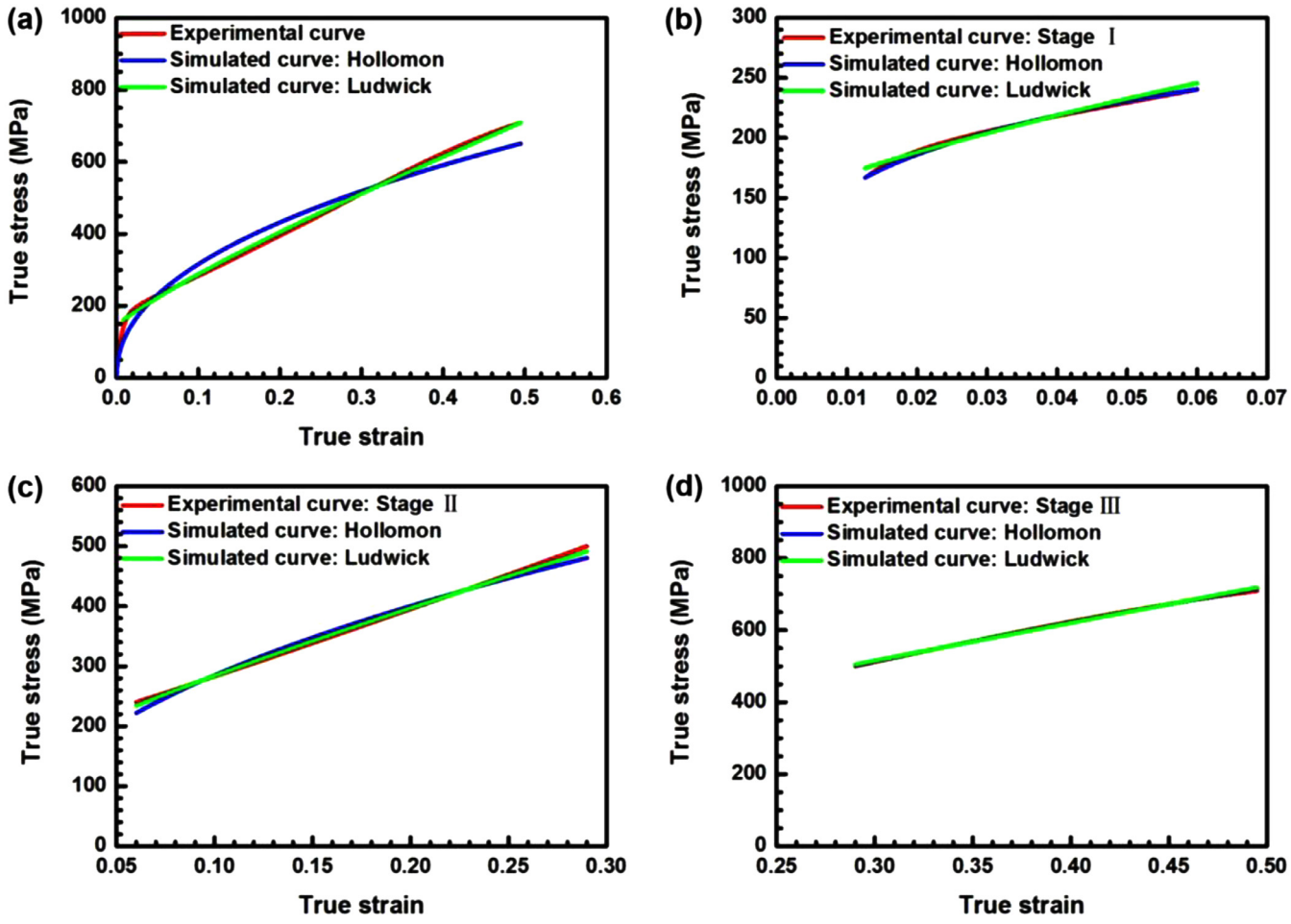

Fig. 3. Experimental true stress–strain curves of $Cr_{26}Mn_{20}Fe_{20}Co_{20}Ni_{14}$ HEA and simulated curves by Hollomon ($\sigma = K\varepsilon_p^n$) and Ludwick ($\sigma = \sigma_0 + K\varepsilon_p^n$) equations at different deformation stages. (a) The overall tensile stage. (b) Stage I. (c) Stage II. (d) Stage III.

dislocation arrays, SFs is another important deformation mechanism in the $Cr_{26}Mn_{20}Fe_{20}Co_{20}Ni_{14}$ HEA at the early deformation stage. As shown in Fig. 5a, the micrometer-sized SFs formed when $\varepsilon = 2\%$, and numerous SFs were found in the grain interior at $\varepsilon = 6\%$ (Fig. 5b). These results demonstrate the feature of planar slip in the HEA in which the alloying effect of five elements with near equal molar ratios effectively decreases the SFE, as calculated by Ref. [25]. The mobile unit dislocations and the fast movement of SFs in this stage account for the low Θ in the initial deformation stage [40], in contrast to metals with high SFE that are strengthened by the dislocation tangles and cross slip.

In stage II, when $\varepsilon = 14\%$ and 22%, the dislocation density and {111}-type slip traces increase accordingly, as shown in Fig. 4c and d. It is worth noting that most dislocations were bent and tangled, and only a small number of dislocations (the inset in Fig. 4c) kept the feature of parallel dislocation arrays, suggesting the coexistence of multiple planar slip and cross slip dislocations. Moreover, twinning appeared to gradually govern the deformation mechanism in stage II, as shown in Fig. 5c and d. Several deformation twins with widths of less than 50 nm appeared in some grains when $\varepsilon = 14\%$ (Fig. 5c), indicating that the resolved shear stress reached the critical stress of twinning in the $Cr_{26}Mn_{20}Fe_{20}Co_{20}Ni_{14}$ HEA. When ε = 22%, the quantity of deformation twins increased significantly, and the thickness of twin belts extended to the micrometer range (Fig. 5d). With increased stress, more $1/6\langle 112\rangle$ partial dislocations might be activated on {111} slip planes acting as nuclei for twins, resulting in increases of both twin number and twin thickness. Twin lamellae usually act as effective obstacles to the motion of dislocations, especially for those with slip systems non-parallel to the twin lamellae [41,42]. Therefore, the deformation twinning dynamically increased the capacity of dislocation accumulation, contributing to the steady-state Θ.

In stage III, when ε = 37%, the {111}-type slip traces still appeared in the majority of grains, and the space between the slip traces was full of dense dislocations, as shown in Fig. 4e. The microscale twin appearing in stage II evolved into nanoscale twin bundles that contained several nanoscale twin lamellae with thicknesses of 10–50 nm, as shown in Fig. 5e. With increased strain, the synchronous stress increase induced the formation of nanoscale twin nuclei within the microscale twin lamellae, resulting in the formation of nanoscale twin bundles. When the tensile specimen was elongated to fracture (ε = 49%), high-density dislocations accumulated and were distributed homogeneously within the twin and matrix lamellae, as shown in Fig. 4f. The homogenously distributed dislocation structures were different from the dislocation cells in other FCC HEAs with low- to medium-SFE [13,22]. Moreover, as can be seen the selected area electron diffraction (SAED) pattern in Fig. 5f, a diffraction ring similar to that seen in polycrystalline materials was observed, which resulted from (i) intersections of extensive primary (T1) and secondary (T2) nanoscale twins, leading to a significant grain refinement (i.e., a dynamic Hall–Petch effect) and (ii) accumulation of dislocations at TBs, leading to TB curvature.

The severe intersections between multiple nanoscale twins caused the lattice distortion, which were characterized as trenches and bulges in the HRTEM images (Fig. 6a and d). Fig. 6b, c, e, and f are magnified

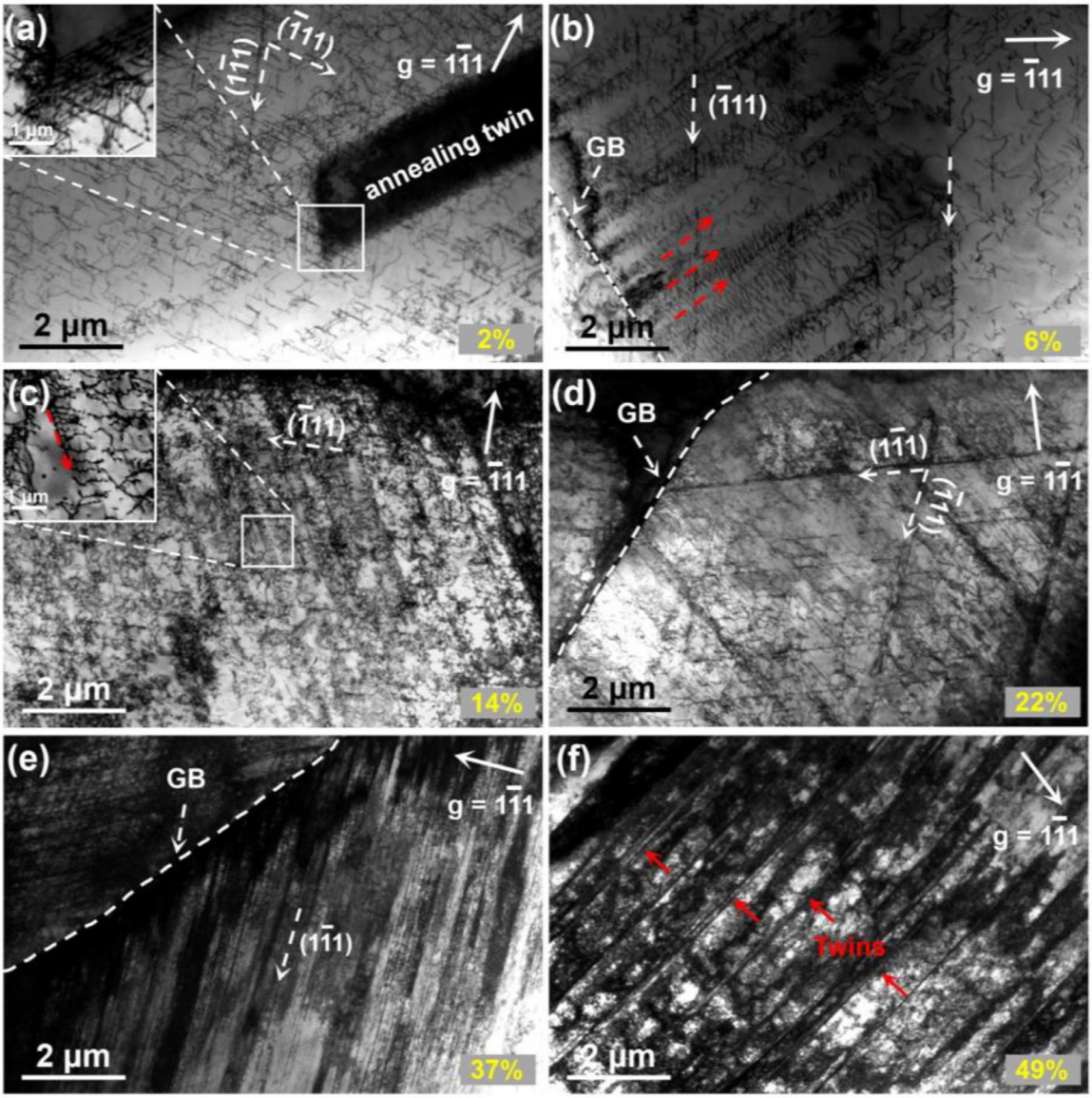

Fig. 4. TEM micrographs with ⟨111⟩ ***g*** vectors of $Cr_{26}Mn_{20}Fe_{20}Co_{20}Ni_{14}$ HEA tensile deformed to different true strains as marked in the lower right corner of each panel. (a–e) {111} slip traces were marked with white dotted arrows and parallel dislocation arrays were marked with red dotted arrows. (f) High-density and homogeneously-distributed dislocations accumulated within twin (marked with red arrows) and matrix lamellae. (For interpretation of the references to colour in this figure legend, the reader is referred to the web version of this article.)

images of the regions "b," "c," "e," and "f" marked with white rectangles in Fig. 6a and d. Nanoscale twins of less than 5 atomic layers and numerous 1/6⟨112⟩ typed SFs (marked with white arrows) on the nanoscale twin boundary and within the nanoscale twins are seen. The numerous SFs on TBs might be residual extensions of nanoscale twins. Another reason for numerous SFs is a dynamic Hall–Petch effect by twinning. When coarse grains are refined into nanometer-sized twin lamellae, the formation of SFs became a dominant deformation mechanism. Previous studies have shown that the activity of SFs is the dominant deformation mechanism in grains less than 10 nm, as the twinning and dislocation slipping become difficult due to the high critical shear stress [43,44].

3.4. Measurement of stacking fault energy

SFE can be measured from peak broadening and shift of x-ray diffraction [45–47], and from SF width imaged by TEM [48] and HRTEM [49]. Here we measured SF width from HRTEM images on [110] zone axis (Z.A.) of the tensile-fractured $Cr_{26}Mn_{20}Fe_{20}Co_{20}Ni_{14}$ HEA with ε = 49%, as shown in Fig. 7. A SF was framed by a red rectangular (Fig. 7a) and the magnfied HRTEM image (Fig. 7b) revealed the SF was formed from the dissociation of an extended 60° dislocation 1/2⟨110⟩ to two 1/6⟨112⟩ partial dislocations (a 90° partial and a 30° partial). The SF width was then measured from the distance between the 90° and 30° partials which are located at the two ends of the SF. Statistic HRTEM measurements indicated that the SF width was about 11 nm. Then the SFE could be calculated by [50]:

$$\gamma = \frac{Gb^2}{2\pi d} \tag{3}$$

where γ is SFE, G is shear modulus, approximately equal to 79.3 GPa [48], b is the magnitude of Burgers vector of 1/6 ⟨112⟩, γ is calculated as about 24 mJ m^{-2}, which is larger than the first-principle calculation [25].

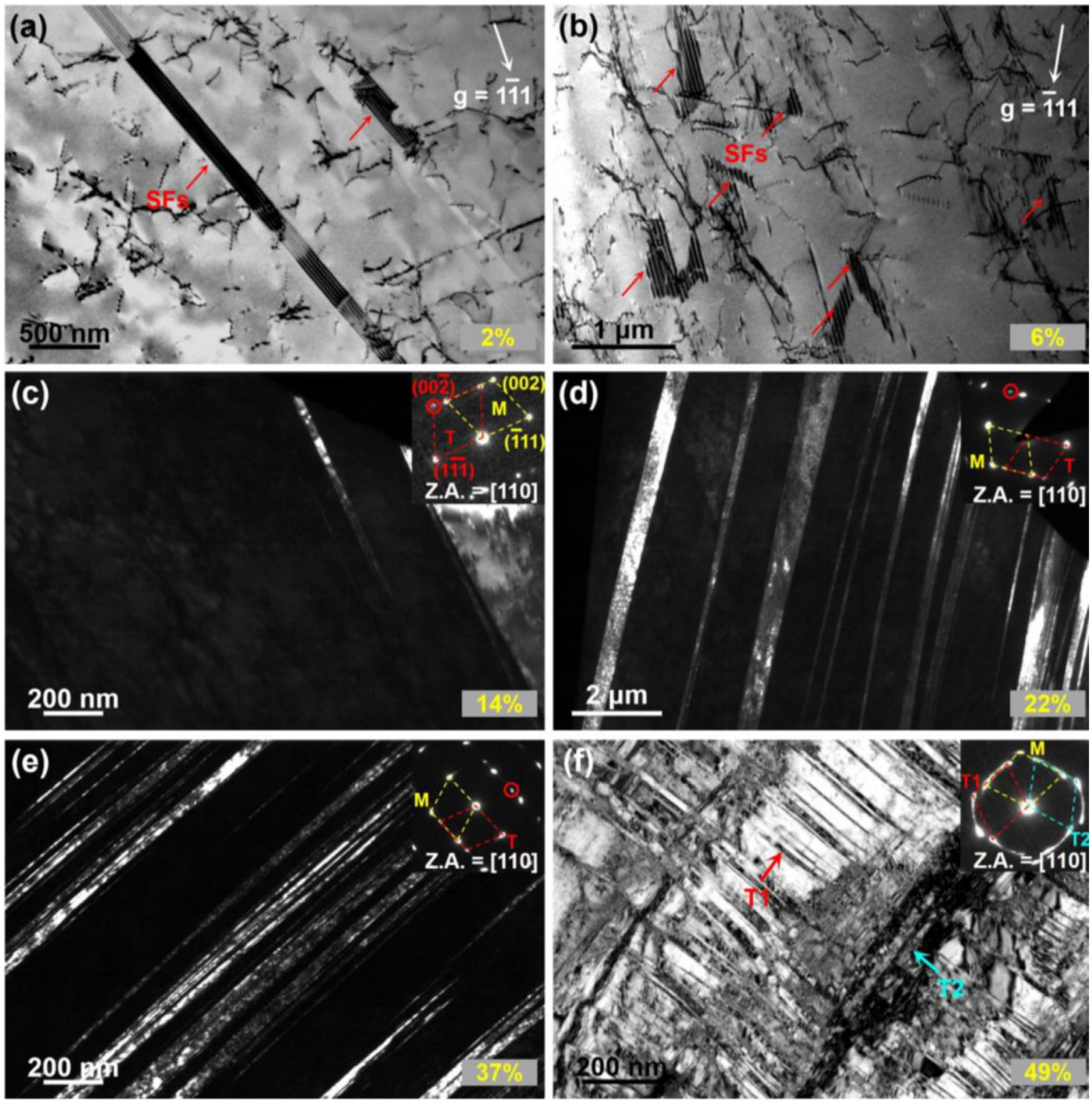

Fig. 5. TEM micrographs on [110] zone axis (Z.A.) showing the evolutions of SFs and twins in the $Cr_{26}Mn_{20}Fe_{20}Co_{20}Ni_{14}$ HEA with different true strains, as marked in the lower right corner of each panel. (a,b) Bright field images of SFs with ⟨111⟩ ***g*** vectors. (c–e) Dark field images with insets of SAED patterns of matrix (marked as "M") and twin (marked as "T"). Diffraction spots circled in red in the SAED patterns were used to obtain the dark field images. (f) Bright field image of deformation twins on two twinning systems (marked as T1 and T2) and the corresponding SAED pattern. (For interpretation of the references to colour in this figure legend, the reader is referred to the web version of this article.)

4. Discussion

4.1. Dislocation strengthening

It has been reported that dislocation accumulation in TWIP alloys is controlled by the SFE [48]. Due to the low SFE, unit dislocation in TWIP alloys tends to slip on parallel slip planes and dissociate into a SF with two Shockley partial dislocations. Cross slip is strongly inhibited by such an extended dislocation core unless this extended core is constricted by external stress with the assistance of thermal activation [48]. Therefore, dislocation multiplication can be enhanced with the suppressed dynamic recovery caused by low SFE. In the $Cr_{26}Mn_{20}Fe_{20}Co_{20}Ni_{14}$ HEA, the low SFE activates planar dislocation arrays and SFs on more parallel {111} slip planes, contributing to a larger accumulation of dislocations than that by a cross slip on multiple slip planes, especially in deformation stages I and II. On the other hand, planar slip decreases the opportunity for dislocation interaction, i.e., weakening the forest hardening effects of dislocations. Besides the typical parallel dislocation arrays, thick and long dislocation tangle lines are also frequently observed in the $Cr_{26}Mn_{20}Fe_{20}Co_{20}Ni_{14}$ HEA. As shown in Fig. 8a, when $\varepsilon = 2\%$, a thick dislocation tangle line traversed a grain and the magnified image reveals that it is composed of dense parallel dislocations. Moreover, the dislocation tangles are thickened by more parallel dislocation lines with increasing true stain from 6% to 14%, as shown in the magnified inset in Fig. 8c. The observed configuration of dislocation tangles composed of parallel dislocations is different from the complex and indistinguishable structures of high dense dislocation walls (HDDWs) reported for other TWIP alloys [22]. Our observation suggests that the dislocation tangles in the $Cr_{26}Mn_{20}Fe_{20}Co_{20}Ni_{14}$ HEA play a weak role in hindering the subsequent slip of dislocations and strain hardening. Nevertheless, the unique atomic structure of HEAs results in new strain hardening mechanisms by the jerky slip of unit dislocations. A recent study of CrMnFeCoNi by in situ TEM revealed that the planar slip is not continuous with extremely low velocity, which formed close-packed dislocation arrays

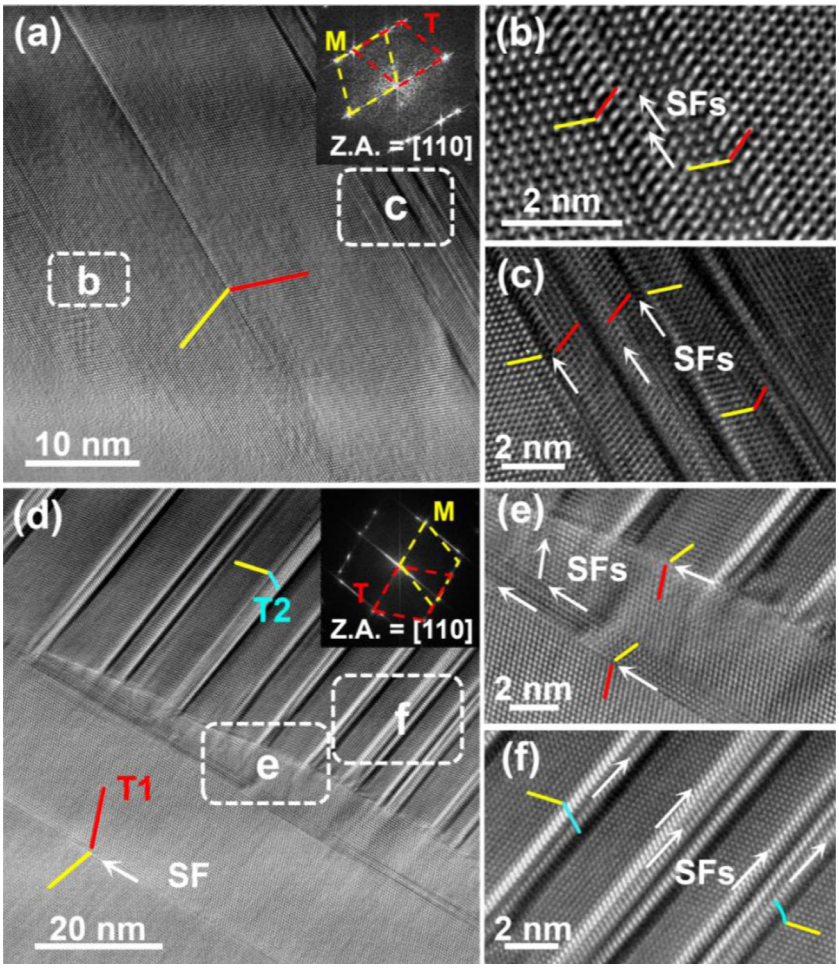

Fig. 6. [110] HRTEM images on [110] zone axis (Z.A.) of the tensile-fractured $Cr_{26}Mn_{20}Fe_{20}Co_{20}Ni_{14}$ HEA with $\varepsilon = 49\%$. (a) Image showing the deformation nanoscale twins on one twinning system (marked by red lines). The inset is the corresponding Fourier transformation (FFT) pattern of matrix (marked as "M") and twin (marked as "T"). (b,c) The magnified images of the regions labeled "b" and "c", respectively, showing the nanoscale twins (marked by red lines), and SFs on the twin boundary (indicated by white arrows). (d) Image showing deformation twins on two twinning systems (T1 and T2). The inset is the corresponding FFT pattern. (e,f) The magnified images of the regions labeled "e" and "f", respectively, showing the nanoscale twins (red and cyan lines) and SFs (white arrows). (For interpretation of the references to colour in this figure legend, the reader is referred to the web version of this article.)

and pile-ups in the activated {111} due to the strong drag effect of solute atoms [51]. Thus, the motion of unit dislocation needs to continuously overcome the activation barriers of the localized bands of slow-moving planar unit dislocations, contributing to an additional increase in strain hardening rate.

According to the classic Taylor hardening model [52], the quantitative forest hardening effect of dislocations in $Cr_{26}Mn_{20}Fe_{20}Co_{20}Ni_{14}$ HEA is given by:

$$\Delta\sigma = M\alpha Gb\sqrt{\rho} \tag{4}$$

where $\Delta\sigma$ is the corresponding increase in the tensile stress, M is the Taylor factor (3.06), α is a constant, G is the shear modulus (79.3 GPa) [48], b is the magnitude of the Burgers vector (0.253 nm), and ρ is the dislocation density. The actual value of α is determined by the geometrical arrangement of the dislocation, and it decreases continuously with deformation. But the variations are in a 10 % range [53], and thus it is approximated as a stable constant during the deformation. In this work, the value of α was 0.45 according to the previous study of CrMnFeCoNi [14]. Here, it is assumed that if no accumulation of dislocations occurred when yield, then the true flow stress σ can be obtained by the corresponding dislocation density ρ at different tensile strains as $\sigma = \Delta\sigma + \sigma_Y$, where σ_y is the yield strength. The statistical values of dislocation density at different tensile strains are smaller than 22% from TEM images and are plotted in Fig. 9a. The dislocation densities are too high to be accurately measured when $\varepsilon > 22\%$. The flow stress was calculated by using ρ values to evaluate the contribution of dislocations for tensile flow stress $\Delta\sigma$. Fig. 9b compares the calculated flow stress with the experimental results, which were in good agreement within the error range, especially at low strain. The difference between the calculated and experimental flow stress increased with the strain, because the contribution of SFs and twins are not considered. In general, the forest dislocation hardening effect is the major mechanism in the initial deformation stage in the $Cr_{26}Mn_{20}Fe_{20}Co_{20}Ni_{14}$ HEA.

4.2. Strengthening by SFs and twins

SFs have routinely been regarded as omens of twins, but unfortunately, the hardening effect of SFs is neglected in most research. In the $Cr_{26}Mn_{20}Fe_{20}Co_{20}Ni_{14}$ HEA, SFs with sizes in the micrometer and sub-micrometer range are found to be an important deformation mechanism, except for the planar slip dislocations that occur in the initial deformation stage. As can be seen in Fig. 10a, when $\varepsilon = 2\%$, several SFs with partial dislocations pairs were cut by a (–111) slip trace and a unit dislocation, indicating interactions between glide dislocations and SFs. Similar results are seen in Fig. 10b, when $\varepsilon = 6\%$, SFs arrays with single visible partial dislocations tangled with unit dislocations on the same slip plane are seen. In fact, Allain et al. [54] observed that the interaction of glide dislocations with SFs contributes mainly to strain hardening in TWIP steels at room temperature and above. Theoretical studies, such as molecular dynamics simulations, show that SFs can prevent the glide of dislocations on slip planes crossing the SF plane and improve the ductility of materials since the dislocations after penetrating SF are glissile, thereby contributing to the subsequent plastic deformation and strain hardening rate [55,56]. In stage III with high strain, numerous SFs are activated on two {111} slip systems, even in the nanoscale twin lamellae, as shown in Fig. 10c and d. The interaction of the two leading partials of the two SFs on two {111} planes forms a

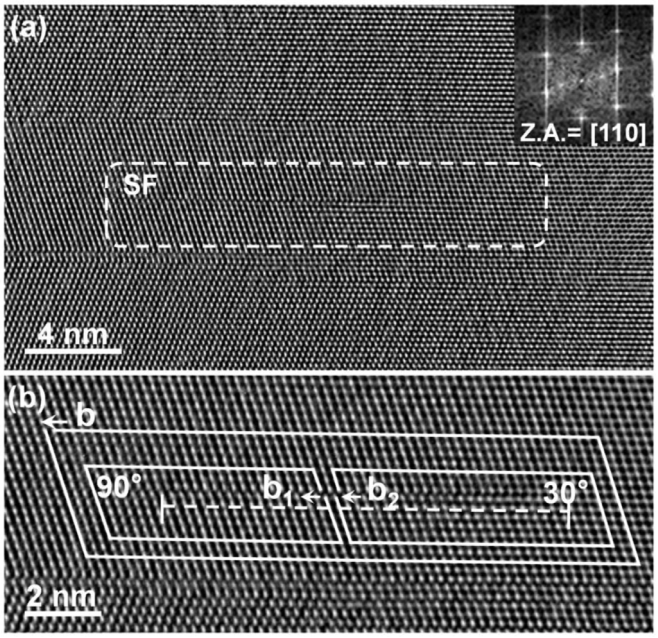

Fig. 7. [110] HRTEM images on [110] zone axis (Z.A.) of the tensile-fractured $Cr_{26}Mn_{20}Fe_{20}Co_{20}Ni_{14}$ HEA with $\varepsilon = 49\%$. (a) HRTEM image containing a SF, as framed by the dotted rectangular. (b) Magnied HRTEM image of the area in the dotted rectangular part in (a) revealing the SF was formed from the dissociation of an extended 60° dislocation $1/2\langle 110\rangle$ to two $1/6\langle 112\rangle$ partial dislocations (a 90° partial and a 30° partial are located at the two ends of the SF), b, b_1 and b_2 are projections of Burgers vectors of the 60° dislocation, 90° and 30° partials.

stair-rod dislocation by:

$$a/6 < 2-1-1 > + a/6 < -121 > \rightarrow a/6 < 110 > \quad (5)$$

The Burgers vector of stair-rod dislocations is perpendicular to the dislocation line and does not lie on either of the two {111} planes of the adjacent SFs. Thus, stair-rod dislocations cannot glide on these {111} planes. Because the {100} plane that contains the stair-rod dislocation line and its Burgers vector is not a slip plane, the stair-rod dislocation is sessile. The stair-rod dislocation acts as a barrier to the glide of further dislocations on the two {111} planes and is known as a Lomer–Cottrell lock [57,58], which certainly leads to the large strain hardening rate of the single-phase FCC HEA. Xu et al. [59] reported that these immobile dislocation locks could act as Frank–Read sources for dislocation multiplication and form parallel long dislocations in the same slip systems, resulting in a liner increase of flow stress with strain.

At high strain levels, twinning governed the deformation mechanisms in the $Cr_{26}Mn_{20}Fe_{20}Co_{20}Ni_{14}$ HEA. So, it is necessary to understand the contribution of TWIP effects to the superior combination of high stress and high ductility. Tremendous efforts have shown that twinning is a universal and significantly enhanced mechanism in HEAs [2,13,22] with low SFE (20–40 mJ m^{-2}). Deformation twins directly contribute to the plastic strain by inducing back stress, the so-called Bauschinger effect [58,59], and by forming obstacles against the dislocation motion, which reduces the mean free path and enhances the dislocation multiplications [60–62]. According to the study of microstructural evolution of TWIP steels after tensile deformation, deformation twinning as well as interactions between TBs and dislocations and common TBs play key roles during deformation [63,64]. The existing twins dynamically reduce the grain size. Thus, initiations of new twins require a higher stress. The mean free path of dislocations is reduced because of the increased density of TBs, resulting in increased stress. Furthermore, as the twin lamellae become thinner, the external stress required for

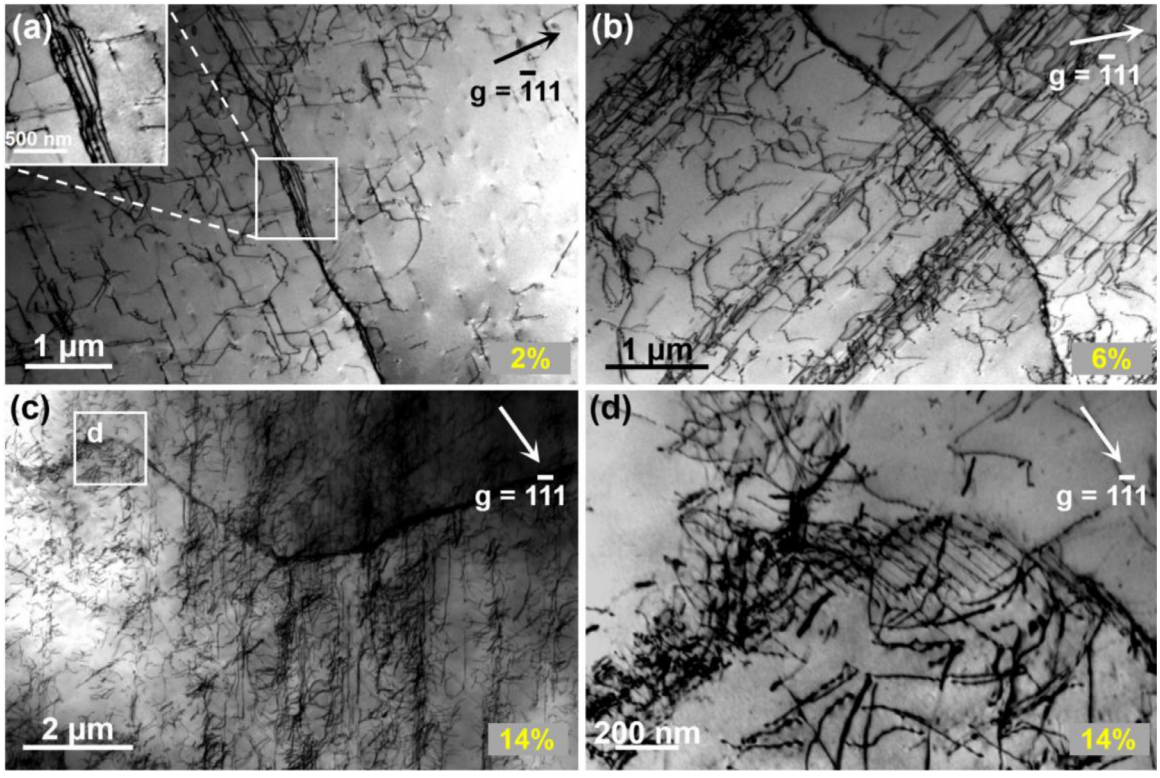

Fig. 8. Bright field TEM images with $\langle 111\rangle$ $\boldsymbol{g}$ vectors showing the structure of dislocation tangles in the $Cr_{26}Mn_{20}Fe_{20}Co_{20}Ni_{14}$ HEA with different true strain values, as marked in the lower right corner of each panel.

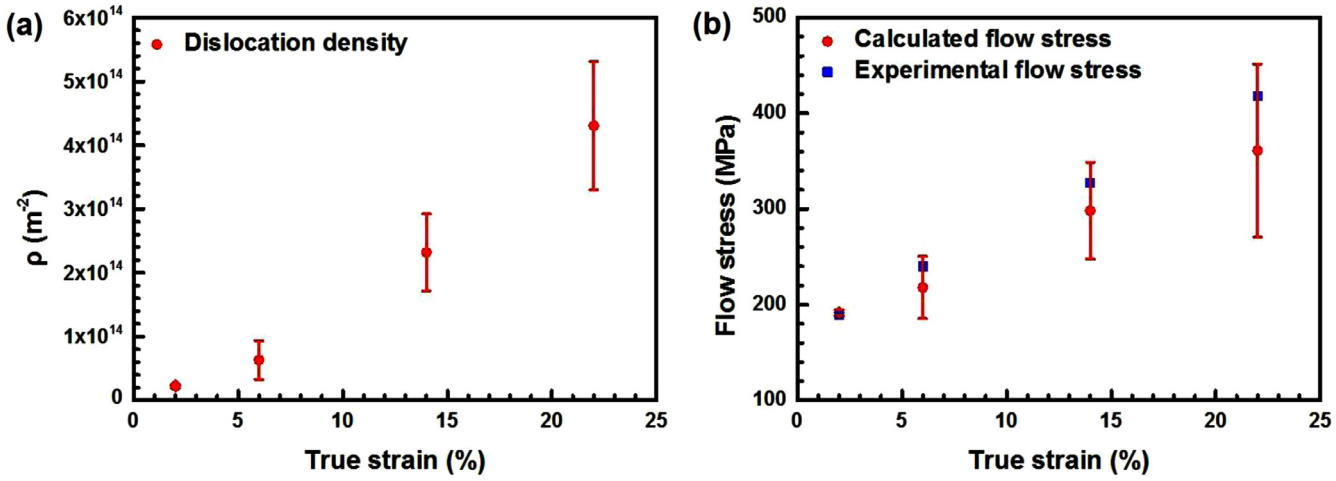

Fig. 9. (a) Dislocation density (ρ) versus true strain. (b) The true flow stress values calculated by the Taylor hardening model and the corresponding experimental values.

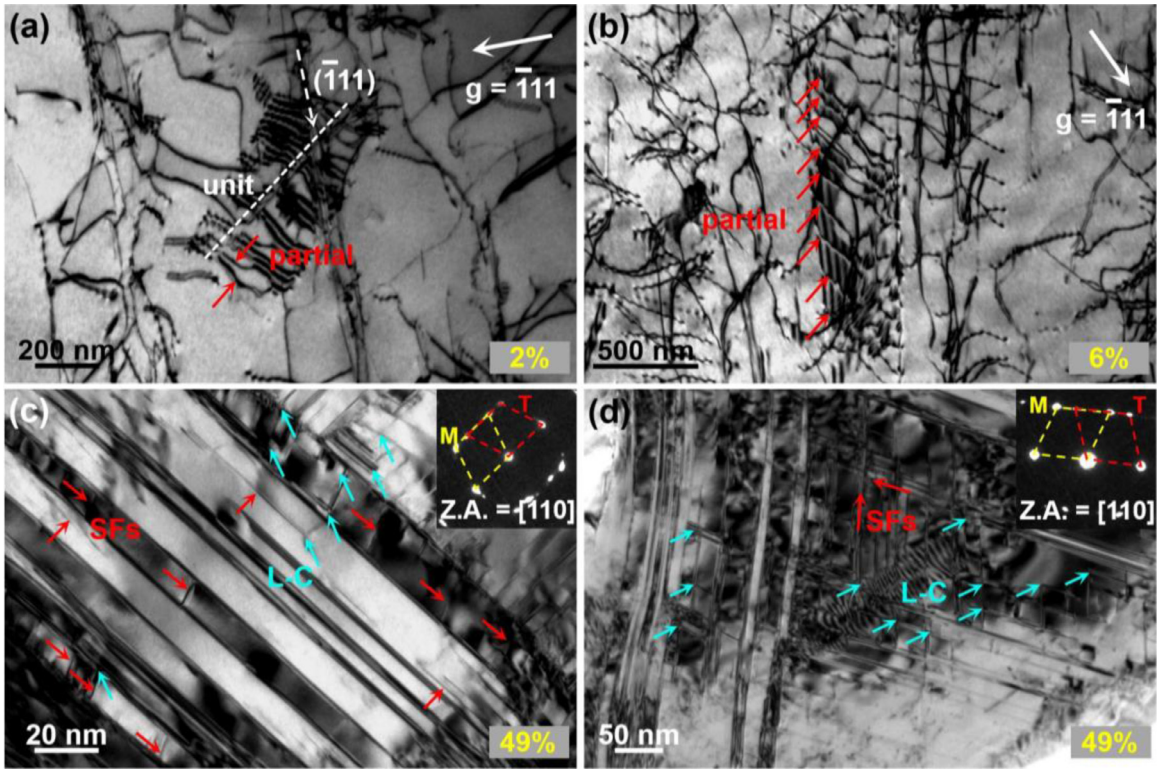

Fig. 10. Bright field TEM images showing the SFs-dislocation and SF–SF interactions in $Cr_{26}Mn_{20}Fe_{20}Co_{20}Ni_{14}$ HEA with different true strain values, as marked in the lower right corner of each panel. (a) Image showing SFs with partial dislocations pairs cut by a (–111) slip trace and a unit dislocation (marked with white dotted arrow and line); (b) Image showing an SF array with single visible partial dislocations tangled with unit dislocations on the same slip plane; (c–d) [110] zone-axis (Z.A.) TEM images showing the SFs (marked with red arrows), inner nanoscale twin lamellae, and the Lomer–Cottrell dislocations (marked with blue arrows) caused by the intersection of SFs on two {111} slip systems. (For interpretation of the references to colour in this figure legend, the reader is referred to the web version of this article.)

dislocations across TBs becomes larger, inhibiting the annihilation of dislocations [65]. Thus, the high strain hardening rate in TWIP alloys can be correlated to the TB-mediated dislocation multiplication and exhaustion process, leading to a concurrent increase in both strength and ductility during plastic straining. It is envisaged that the flow stress increases because the newly formed twins refine the grain size and introduce fresh obstacles. Thus, the propagation of deformation twinning is regarded as a dynamic Hall–Petch effect, which is a determining factor in the strain hardening behavior of twinned microstructures [66].

4.3. Strengthening by sub-grain boundary and phase boundary

The last strengthening factors in our HEA are subgrain boundaries (SGBs) and phase boundaries. As shown in Fig. 11a for the tensile-fractured HEA specimen, a region is divided by an obvious SGB) ("b" area) and phase boundary ("c" area), which are neighboring several nanoscale twins. With careful observation of the high magnification image in Fig. 11b, 4°–14° SGBs were formed by the accumulation of dense SFs, resulting in a severe stress concentration and lattice

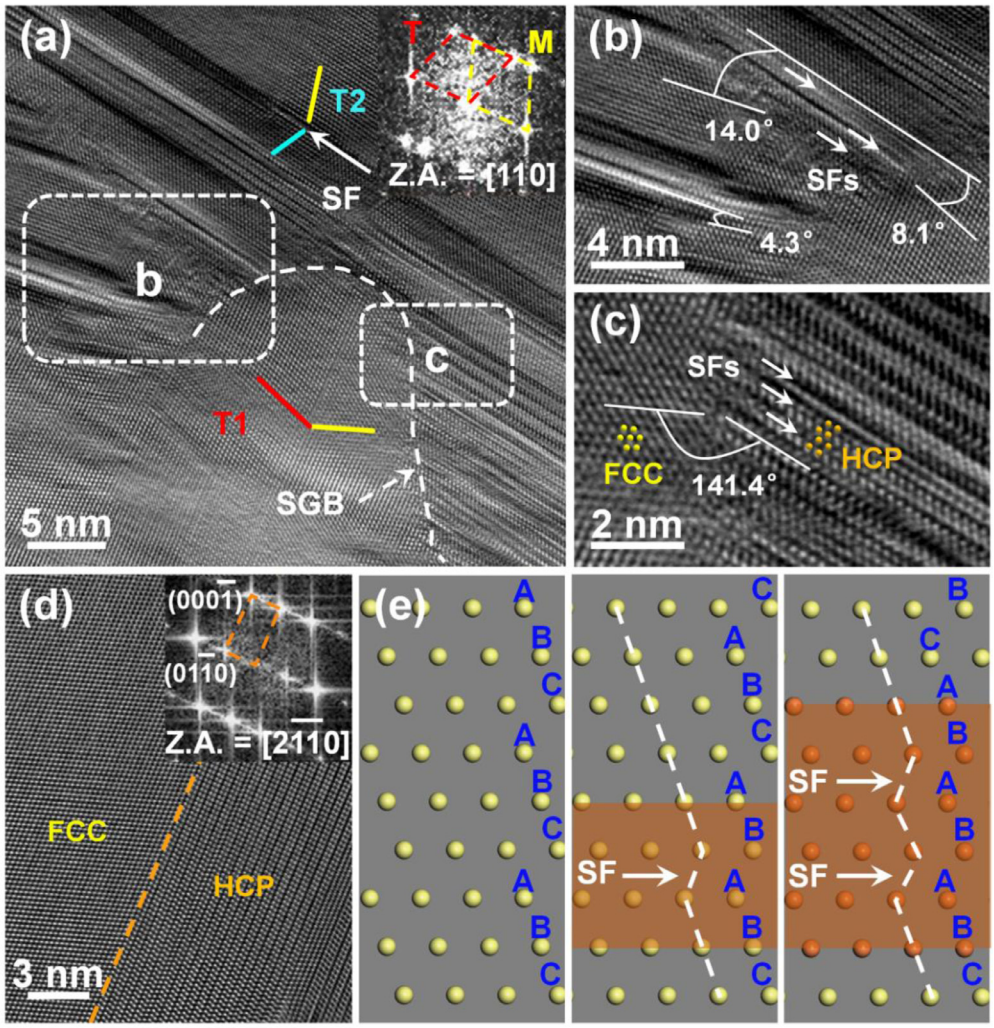

Fig. 11. (a) A [110] zone axis (Z.A.) HRTEM image showing the subgrain boundary and phase boundary in the regions labeled "b" and "c", respectively (outlined by white dotted lines) in the tensile fractured $Cr_{26}Mn_{20}Fe_{20}Co_{20}Ni_{14}$ HEA with 49% true strain. The inset is the corresponding Fourier transformation (FFT) pattern of matrix (marked as "M") and twin (marked as "T"). (b) The magnification of region "b" from panel (a) showing the 4°–14° SGBs by accumulation of SFs. (c) The magnification of region "c" from panel (a) showing the phase boundary between the FCC matrix and nanoscale HCP phase. The adjacent double SFs act as nuclei for the nanoscale HCP phase lamellae. (d) The transient phase boundary (denoted by the orange dotted line) between the FCC and HCP phases. The inset shows the corresponding Fourier transformation pattern of the HCP phase. (e) Schematic atomic formation mechanisms of the HCP phase from the FCC phase via alternate SF emissions.

distortion. Thus, the SGBs could act as barriers for the subsequent dislocation slip and the nuclei of new SFs and nanoscale twins, contributing to the synergistic increase of stress and ductility. It's worth noting that, the lattice distortion in $Cr_{26}Mn_{20}Fe_{20}Co_{20}Ni_{14}$ HEA is different from the observations of kinks and bends in the lattice layers in NbMoTaW HEA caused by the large difference between atomic radii, which induces non-uniform stress fields and a dynamic drag effect of dislocations sliding along a distorted lattice, leading to increased strengthening.

Besides the SGBs, a coherent phase boundary of FCC phase and HCP phase is also observed in area "c" in Fig. 11a. Fig. 11c shows that HCP laths form in the original nanoscale twins, nucleated by the adjacent double SFs. The HCP laths have a consistent orientation to the nanoscale twins and share the same {111} habit planes as the TBs, i.e., forming a 141° angle with the FCC matrix, as shown by the Fourier tranformation pattern of the high-resolution TEM (Fig. 11d). The HCP lamellae would also be very effective barriers for dislocation slip since transmission of edge-component dislocations into the HCP phase would require the activation of dislocations with a component along [0001], requiring either $\langle \boldsymbol{c} \rangle$ or $\langle \boldsymbol{c} + \boldsymbol{a} \rangle$ dislocations [67]. Moreover, the increased phase boundary density due to transformation creates additional obstacles to dislocation slip, thereby contributing to the strain hardening and the synergic deformation of the two phases, leading to a highly beneficial dynamic strain–stress partitioning effect and enhancing the synchronous increase of strength and ductility [2].

A typical 1/6⟨112⟩ Shockley partial dislocation was observed and demonstrated atomic formation mechanisms of the HCP phase from the FCC phase via alternate SF emissions as schematically represented in Fig. 11e. Nine atomic layers in the FCC matrix with an atomic packed order of ABCABCABC were inspected. As shown in Fig. 11e, when an atomic layer was displaced by a Shockley partial dislocation, an SF was introduced with a stacking sequence of CABCABABC, namely a thin HCP phase lamella with four atomic layers of ABAB. When another Shockley dislocation moved on the alternate (not adjacent) close-packed plane, the double alternate SFs exhibited an atomic packed sequence corresponding to BCABABABC, namely an HCP phase with six atomic layers. Therefore, the HCP phase transformation of the $Cr_{26}Mn_{20}Fe_{20}Co_{20}Ni_{14}$ HEA at room temperatures was realized via alternate SF emissions.

5. Conclusion

In this study, we prepared a $Cr_{26}Mn_{20}Fe_{20}Co_{20}Ni_{14}$ HEA with a SEF of 3.5 mJ m^{-2} and a fully recrystallized equiaxed grains with a size of ~50 μm by making an appropriate component adjustment based on the equiatomic CoCrFeMnNi alloy to promote twinning. Tensile testing indicated that the HEA possesses an excellent combination of high strength and high ductility. The post-deformed samples at different strain levels were further analyzed by TEM and HRTEM to reveal the deformation and strengthening mechanisms. The main conclusions are as follows:

1. The mechanical properties of $Cr_{26}Mn_{20}Fe_{20}Co_{20}Ni_{14}$ HEA were comparable to the equiatomic CoCrFeMnNi alloy due to the three-stage strain hardening behavior. The average strain hardening exponent n simulated by the Hollomon equation and the Ludwick equation were 0.46 and 0.85, respectively.

2. Post-deformation analyses on different strain levels revealed planar slip with parallel dislocation arrays and SFs as the major deformation mechanisms in the initial deformation stage; furthermore, twins started to appear at 14% true strain and gradually governed the subsequent deformation behavior.
3. The forest dislocation hardening effect, calculated by the Taylor hardening model, was the major hardening contributor in the initial deformation stage. In addition, the interactions of glide dislocations with SFs, and SFs-SFs interactions (i.e. the sessile Lomer–Cottrell locks) were important strengthening mechanisms. At high strain levels, a Bauschinger effect and a dynamic Hall–Petch effect caused by twinning, sub-grain boundary and phase boundary were dominant strain hardening factors of the $Cr_{26}Mn_{20}Fe_{20}Co_{20}Ni_{14}$ HEA.

Declaration of Competing Interest

The authors declare that they have no known competing financial interests or personal relationships that could have appeared to influence the work reported in this paper.

Acknowledgments

Y.H. Zhao and Y.P. Lu acknowledge financial supports from the Fundamental Research Funds for the Central Universities (No. 30919011405), National Key R&D Program of China (Grant No. 2017YFA0204403) and the National Natural Science Foundation of China (Grant Nos. 51822402 and 51225102) as well as supported by the fund of the State Key Laboratory of Solidification Processing in NWPU (Grant No. SKLSP201902).

References

[1] Z.F. Lei, X.J. Liu, Y. Wu, H. Wang, S.H. Jiang, S.D. Wang, X.D. Hui, Y.D. Wu, B. Gault, P. Kontis, D. Raabe, L. Gu, Q.H. Zhang, H.W. Chen, H.T. Wang, J.B. Liu, K. An, Q.S. Zeng, T.G. Nieh, Z.P. Lu, Enhanced strength and ductility in a high-entropy alloy via ordered oxygen complexes, Nature 563 (2018) 546–550.
[2] Z. Li, K.G. Pradeep, Y. Deng, D. Raabe, C.C. Tasan, Metastable high-entropy dual-phase alloys overcome the strength-ductility trade-off, Nature 534 (2016) 227–230.
[3] B. Gludovatz, A. Hohenwarter, D. Catoor, E.H. Chang, E.P. George, R.O. Ritchie, A fracture-resistant high-entropy alloy for cryogenic applications, Science 345 (2014) 1153–1158.
[4] L.J. Santodonato, Y. Zhang, M. Feygenson, C.M. Parish, M.C. Gao, R.J.K. Weber, J.C. Neuefeind, Z. Tang, P.K. Liaw, Deviation from high-entropy configurations in the atomic distributions of a multi-principal-element alloy, Nat. Commun. 6 (2015) 5964.
[5] J.W. Yeh, S.K. Chen, S.J. Lin, J.Y. Gan, T.S. Chin, T.T. Shun, C.H. Tsau, S.Y. Chang, Nanostructured high-entropy alloys with multiple principal elements: novel alloy design concepts and outcomes, Adv. Eng. Mater. 6 (2004) 299–303.
[6] B. Cantor, I.T.H. Chang, P. Knight, A.J.B. Vincent, Microstructural development in equiatomic multicomponent alloys, Mater. Sci. Eng. A 375–377 (2004) 213–218.
[7] Y. Zhang, T.T. Zuo, Z. Tang, M.C. Gao, K.A. Dahmen, P.K. Liaw, Z.P. Lu, Microstructures and properties of high-entropy alloys, Prog. Mater. Sci. 61 (2014) 1–93.
[8] M.J. Yao, K.G. Pradeep, C.C. Tasan, D. Raabe, A novel single phase non-equiatomic FeMnNiCoCr high-entropy alloy with exceptional phase stability and tensile ductility, Scr. Mater. 72–73 (2014) 5–8.
[9] O.N. Senkov, J.M. Scott, S.V. Senkova, D.B. Miracle, C.F. Woodward, Microstructure and room temperature properties of a high-entropy TaNbHfZrTi alloy, J. Alloy. Compd. 509 (2011) 6043–6048.
[10] A. Takeuchi, K. Amiya, T. Wada, K. Yubuta, W. Zhang, High-entropy alloys with a hexagonal close-packed structure designed by equi-atomic alloy strategy and binary phase diagrams, JOM 66 (2014) 1984–1992.
[11] K.Y. Tsai, M.H. Tsai, J.W. Yeh, Sluggish diffusion in Co-Cr-Fe-Mn-Ni high-entropy alloys, Acta Mater 61 (2013) 4887–4897.
[12] P.P. Bhattacharjee, G.D. Sathiaraj, M. Zaid, J.R. Gatti, C. Lee, C.W. Tsai, J.W. Yeh, Microstructure and texture evolution during annealing of equiatomic CoCrFeMnNi high-entropy alloy, J. Alloy. Compd. 587 (2014) 544–552.
[13] F. Otto, A. Dlouhý, Ch. Somsen, H. Bei, G. Eggeler, E.P. George, The influence of temperature and microstructure on the tensile properties of a CoCrFeMnNi high-entropy alloy, Acta Mater. 61 (2013) 5743–5755.
[14] G. Laplanche, A. Kostka, O.M. Horst, G. Eggeler, E.P. George, Microstructure evolution and critical stress for twinning in the CrMnFeCoNi high-entropy alloy, Acta Mater. 118 (2016) 152–163.
[15] Z. Zhang, M.M. Mao, J. Wang, B. Gludovatz, Z. Zhang, S.X. Mao, et al., Nanoscale origins of the damage tolerance of the high-entropy alloy CrMnFeCoNi, Nat. Commun. 6 (2015) 10143.
[16] B. Gludovatz, A. Hohenwarter, K.V.S. Thurston, H. Bei, Z. Wu, E.P. George, R.O. Ritchie, Exceptional damage-tolerance of a medium-entropy alloy CrCoNi at cryogenic temperatures, Nat. Commun. 7 (2016) 10602.
[17] L. Remy, A. Pineau, Twinning and strain-induced F.C.C.-H.C.P. transformation in the FeMnCrC system, Mater. Sci. Eng. 28 (1977) 99–107.
[18] A. Saeed-Akbari, et al., Characterization and prediction of flow behavior in high-manganese twinning induced plasticity steels: Part I. Mechanism maps and work-hardening behavior, Metall. Mater. Trans. A 43 (2012) 1688–1704.
[19] S. Allain, et al., Correlations between the calculated stacking fault energy and the plasticity mechanisms in Fe–Mn–C alloys, Mater. Sci. Eng. A 387–389 (2004) 158–162.
[20] V. Shterner, I.B. Timokhina, H. Beladi, On the work-hardening behavior of a high manganese TWIP steel at different deformation temperatures, Mater. Sci. Eng. A 669 (2016) 437–446.
[21] S. Curtze, V.T. Kuokkala, Dependence of tensile deformation behavior of TWIP steels on stacking fault energy, temperature and strain rate, Acta Mater 58 (2010) 5129–5141.
[22] Y. Deng, C.C. Tasan, K.G. Pradeep, H. Springer, A. Kostka, D. Raabe, Design of a twinning-induced plasticity high entropy alloy, Acta Mater 94 (2015) 124–133.
[23] Z.M. Li, F. Körmann, B. Grabowski, J. Neugebauer, D. Raabe, Ab initio assisted design of quinary dual-phase high-entropy alloys with transformation-induced plasticity, Acta Mater 136 (2017) 262–270.
[24] Z.M. Li, C.C. Tasan, H. Springer, B. Gault, D. Raabe, Interstitial atoms enable joint twinning and transformation induced plasticity in strong and ductile high-entropy alloys, Sci. Rep. 7 (2017) 40704.
[25] A.J. Zaddach, C. Niu, C.C. Koch, D.L. Irving, Mechanical properties and stacking fault energies of NiFeCrCoMn high-entropy alloy, JOM 65 (2013) 1780.
[26] O. Dmitrieva, D. Ponge, G. Lnden, J. Millán, P. Choi, J. Sietsma, D. Raabe, Chemical gradient across phase boundaries between martensite and austenite in steel studied by atom probe tomography and simulation, Acta Mater 59 (2011) 364–374.
[27] D. Raabe, S. Sandlöbes, J. Millán, D. Ponge, H. Assadi, M. Herbig, P.P. Choi, Segregation engineering enables nanoscale martensite to austenite phase transformation at grain boundaries: A pathway to ductile martensite, Acta Mater 61 (2013) 6132–6152.
[28] M. Kuzmina, D. Ponge, D. Raabe, Grain boundary segregation engineering and austenite reversion turn embrittlement into toughness: Example of a 9 wt.% medium Mn steel, Acta Mater 86 (2015) 182–192.
[29] Z.G. Wu, Y.F. Gao, H.B. Bei, Thermal activation mechanisms and Labusch-type strengthening for a family of high-entropy and equiatomic solid-solution alloys, Acta Mater 120 (2016) 108–119.
[30] Y.H. Zhao, J.F. Bingert, Y.T. Zhu, X.Z. Liao, R.Z. Valiev, Z. Horita, T.G. Langdon, Y.Z. Zhou, E.J. Lavernia, Tougher ultrafine grain Cu via high-angle grain boundaries and low dislocation density, Appl. Phys. Lett. 92 (2008) 081903.
[31] Y.H. Zhao, Y.T. Zhu, E.J. Lavernia, Strategies for improving tensile ductility of bulk nanostructured materials, Adv. Eng. Mater. 12 (2010) 769–778.
[32] O. Bouaziz, S. Allain, C.P. Scott, P. Cugy, D. Barbier, High manganese austenitic twinning induced plasticity steels: A review of the microstructure properties relationships, Curr. Opin. Solid State Mater. Sci. 15 (2011) 141–168.
[33] Y.J. Wei, Y.Q. Li, L.C. Zhu, Y. Liu, X.Q. Lei, G. Wang, Y.X. Wu, Z.L. Mi, J.B. Liu, H.T. Wang, H.J. Gao, Evading the strength–ductility trade-off dilemma in steel through gradient hierarchical nanotwins, Nat. Commun. 5 (2014) 3580.
[34] X.L. Wu, P. Jiang, L. Chen, F.P. Yuan, Y.T. Zhu, Extraordinary strain hardening by gradient structure, PNAS 112 (2015) 7197–7201.
[35] T.H. Courney, in: Mechanical Behavior of Materials, 2nd ed., McGraw-Hill. Company, 2000, p. 13.
[36] X.L. Wu, M.X. Yang, F.P. Yuan, L. Chen, Y.T. Zhu, Combining gradient structure and TRIP effect to produce austenite stainless steel with high strength and high ductility, Acta Mater. 112 (2016) 337–346.
[37] M.M. Wang, C.C. Tasan, D. Ponge, D. Raabe, Spectral TRIP enables ductile 1.1 GPa martensite, Acta Mater 111 (2016) 262–272.
[38] Z.C. Li, R.D.K. Misra, Z.H. Cai, H.X. Li, H. Ding, Mechanical properties and deformation behavior in hot-rolled 0.2C-1.5/3Al-8.5Mn-Fe TRIP steel: The discontinuous TRIP effect, Mater. Sci. Eng. A 673 (2016) 63–72.
[39] E.W. Hart, Theory of the tensile test, Acta Mater. 15 (1967) 351–355.
[40] Q. Wei, S. Cheng, K.T. Ramesh, E. Ma, Effect of nanocrystalline and ultralfine grain sizes on the strain rate sensitivity and activation volume: fcc versus bcc metals, Mater. Sci. Eng. A 381 (2004) 71–79.
[41] L. Lu, X. Chen, X. Huang, K. Lu, Strengthening materials by engineering coherent internal boundaries at the nanoscale, Science 323 (2009) 607–610.
[42] K. Lu, L. Lu, S. Suresh, Strengthening materials by engineering coherent internal boundaries at nanoscale, Science 324 (2009) 349–352.
[43] Y.T. Zhu, X.Z. Liao, X.L. Wu, J. Narayan, Grain size effect on deformation twinning and detwinning, J. Mater. Sci. 48 (2013) 4467–4475.
[44] Y.T. Zhu, X.Z. Liao, X.L. Wu, Deformation twinning in nanocrystalline materials, Prog. Mater. Sci. 57 (2012) 1–62.
[45] B. Cai, B. Liu, S. Kabra, et al., Deformation mechanisms of Mo alloyed Fe-CoCrNi high entropy alloy In situ neutron diffraction, Acta Mater. 127 (2017) 471–480.
[46] J.S. Jeong, W. Woo, K.H. Oh, et al., In situ neutron diffraction study of the microstructure and tensile deformation behavior in Al-added high manganese austenitic steels, Acta Mater. 60 (2012) 2290–2299.
[47] S. Harjo, Y. Tomota, P. Lukáš, et al., In situ neutron diffraction study of α–γ Fe–Cr–Ni alloys under tensile deformation, Acta Mater. 49 (2001) 2471–2479.
[48] N.L. Okamoto, et al., Size effect, critical resolved shear stress, stacking fault energy, and solid solution strengthening in the CrMnFeCoNi high-entropy alloy, Sci. Rep. 6 (2016) 35863.

[49] T.M. Smith, M.S. Hooshmand, B.D. Esser, F. Otto, D.W. McComb, E.P. George, M. Ghazisaeidi, M.J. Mills, Atomic-scale characterization and modelling of 60° dislocation in a high-entropy alloy, Acta Mater. 110 (2016) 252–363.
[50] D. Hull, D.J. Bacon, in: Introduction to Dislocations, 5th Edition, Elsivier, 2011, pp. 89–90.
[51] G. Laplanche, A. Kostka, C. Reinhart, J. Hunfeld, G. Eggeler, E.P. George, Reasons for the superior mechanical properties of medium-entropy CrCoNi compared to high--entropy CrMnFeCoNi, Acta Mater. 128 (2017) 292–303.
[52] J.K. Kim, B.C. De Cooman, Stacking fault energy and deformation mechanism in Fe-xMn-0.6C-yAl TWIP steel, Mater. Sci. Eng. A 676 (2016) 216–231.
[53] W. Püschl, Models for dislocation cross-slip in close-packed crystal structures: a critical review, Prog. Mater. Sci. 47 (2002) 415–461.
[54] S. Allain, et al., Correlations between the calculated stacking fault energy and the plasticity mechanisms in Fe–Mn–C alloys, Mater. Sci. Eng. A 387–389 (2004) 158–162.
[55] H. Mecking, U.F. Kocks, Kinetics of flow and strain-hardening, Acta Metall. 29 (1981) 1865–1875.
[56] U.F. Kocks, H. Mecking, Physics and phenomenology of strain hardening: the FCC case, Prog. Mater. Sci. 48 (2003) 171–273.
[57] J. Yoo, K. Choi, A. Zargaran, N.J. Kim, Effect of stacking faults on the ductility of Fe-18Mn-1.5Al-0.6C twinning-induced plasticity steel at low temperatures, Scr. Mater. 137 (2017) 18–21.
[58] D. Hull, D.J. Bacon, in: Introduction to Dislocation, University of Liverpool, Liverpool, 2011, pp. 99–102.
[59] X.D. Xu, P. Liu, Z. Tang, A. Hirata, S.X. Song, T.G. Nieh, P.K. Liaw, C.T. Liu, M.W. Chen, Transmission electron microscopy characterization of dislocation structure in a face-centered cubic high-entropy alloy $Al_{0.1}$CoCrFeNi, Acta Mater. 144 (2018) 107–115.
[60] O. Bouaziz, S. Allain, C. Scott, Effect of grain and twin boundaries on the hardening mechanisms of twinning-induced plasticity steels, Scr. Mater. 58 (2008) 484–487.
[61] M. Huang, et al., Modelling the effect of carbon on deformation behavior of twinning induced plasticity steels, J. Mater. Sci. (2011) 1–5.
[62] V. Shterner, I.B. Timokhina, H. Beladi, On the work-hardening behavior of a high manganese TWIP steel at different deformation temperatures, Mater. Sci. Eng. A 669 (2016) 437–446.
[63] I. Karaman, et al., Deformation of single crystal Hadfield steel by twinning and slip, Acta Mater. 48 (2000) 1345–1359.
[64] O. Bouaziz, N. Guelton, Modelling of TWIP effect on work-hardening, Mater. Sci. Eng. A 319–321 (2001) 246–249.
[65] K. Jeong, J.E. Jin, Y.S. Jung, S. Kang, Y.K. Lee, The effects of Si on the mechanical twinning and strain hardening of Fe-18Mn-0.6C twinning-induced plasticity steel, Acta Mater. 61 (2013) 3399–3410.
[66] D.R. Steinmetz, T. Jäpel, B. Wietbrock, P. Eisenlohr, I. Gutierrez-Urrutia, et al., Revealing the strain-hardening behavior of twinning-induced plasticity steels: Theory, simulations, experiments, Acta Mater 61 (2013) 494–510.
[67] J. Miao, C.E. Slone, T.M. Smith, C. Niu, H. Bei, M. Ghazisaeidi, G.M. Pharr, M.J. Mills, The evolution of the deformation substructure in a Ni-Co-Cr equiatomic solid solution alloy, Acta Mater. 132 (2017) 35–48.